

An Adiabatic Mechanism for the Reduction of Jet Meander Amplitude by Potential Vorticity Filamentation

Ben Harvey, John Methven and Maarten H. P. Ambaum

Abstract

The amplitude of ridges in large-amplitude Rossby waves have been shown to decrease systematically with lead time during the first 1–5 days of operational global numerical weather forecasts. These models also exhibit a rapid reduction in the isentropic gradient of potential vorticity (PV) at the tropopause during the first 1–2 days of forecasts. This paper identifies a mechanism linking the reduction in large-scale meander amplitude on jet streams to declining PV gradients. The mechanism proposed is that a smoother isentropic transition of PV across the tropopause leads to excessive PV filamentation on the jet flanks and a more lossy waveguide. The approach taken is to analyse Rossby wave dynamics in a single-layer quasi-geostrophic model. Numerical simulations show that the amplitude of a Rossby wave propagating along a narrow but smooth PV front do indeed decay transiently with time. This process is explained in terms of the filamentation of PV from the jet core and associated absorption of wave activity by the critical layers on the jet flanks, and a simple method for quantitatively predicting the magnitude of the amplitude reduction without simulation is presented. Explicitly-diffusive simulations are then used to show that the combined impact of diffusion and the adiabatic rearrangement of PV can result in a decay rate of Rossby waves which is 2–4 times faster than could be expected from diffusion acting alone. This predicted decay rate is sufficient to explain the decay observed in operational weather forecasting models.

1 Introduction

Rossby waves are a ubiquitous feature of the extratropical atmosphere, as evidenced by the perpetual north-south meandering of the mid-latitude jet streams. Due to the dominant dynamical role they play in the large-scale evolution of the atmosphere, including extratropical cyclone development, blocking episodes and teleconnection patterns, a good representation of Rossby waves is a crucial requirement for accurate simulations in both numerical weather prediction (NWP) and climate models.

The jet streams and associated Rossby waves reside on the large isentropic gradient of potential vorticity (PV) at the tropopause (Hoskins et al., 1985). Using operational forecast data from recent winters, Gray et al. (2014) showed that global NWP models exhibit a pair of systematic biases associated with these features. First, a fast reduction of the isentropic gradient of PV at the tropopause occurs during the first 1–2 days of forecasts. That is, the transition from low PV tropospheric air to high PV stratospheric air on an isentropic surface becomes less sharp with lead time. Second, a more gradual

reduction of the amplitude of Rossby waves, as measured by the amplitude of ridges, occurs during the first 1–5 days of forecasts meaning the north-south meandering of the jet stream becomes too weak. A likely cause for the first of the biases is the limited spatial resolution of the numerical models, meaning the sharp PV gradients in analyses cannot be maintained in time. However, parametrized physical processes such as radiative and diabatic heating also act, on average, to sharpen the PV gradient at the tropopause (Chagnon et al., 2013; Saffin et al., 2017), so any errors in their representation in the models may also contribute to the bias.

A key question is to understand the extent to which the exact representation of the sharpness of the tropopause impacts the large-scale evolution of Rossby waves. Harvey et al. (2016) investigated the impact of tropopause sharpness on Rossby wave phase and group speeds using a simple single-layer quasi-geostrophic (QG) model, and showed that a gradient of PV at the tropopause that is too smooth is expected to reduce both the maximum jet speed and the rate at which Rossby waves can counter-propagate upstream. In terms of the net change in Rossby wave speed, these two effects cancel each other at first order. However, the reduction in jet speed always dominates at second order meaning the phase speed of Rossby waves can be expected to be systematically less positive (i.e. less eastward) if the isentropic transition of PV at the tropopause is smoother than observed.

A possible mechanism for the second systematic model bias, the gradual reduction in Rossby wave amplitudes during the first 1–5 days of forecasts, is the misrepresentation of diabatic processes in numerical models. In particular, the latent heat released in the warm conveyor belts of extratropical cyclones is likely an important contributor to the amplitude of Rossby waves since the outflow at upper-tropospheric levels acts to increase the mass of air within upper-tropospheric ridges (Grams et al., 2011; Madonna et al., 2014; Martínez-Alvarado et al., 2016), and the divergent outflow also advects the tropopause PV gradient further polewards (Grams & Archambault, 2016). This was one of the motivations behind the recent North Atlantic Waveguide and Downstream Impacts Experiment (NAWDEX) field campaign, which used multiple aircraft to measure jet stream and cloud structures, and their relation to diabatic processes, in the North Atlantic region during autumn 2016 (Schäfler et al., 2018).

In the present study, an alternative explanation for the amplitude reduction is explored. The hypothesis is that the fast reduction of the isentropic gradient of PV at the tropopause during the first 1–2 days of forecasts may subsequently *cause* the reduction of Rossby wave amplitudes. The mechanism proposed is that filamentation of PV on the flanks of the jet is enhanced if the transition of PV across the tropopause is smoothed, and this feeds back on the large-scale flow as a reduction in the amplitude of jet meanders. In effect, the smoother isentropic transition of PV across the tropopause leads, transiently, to a more lossy waveguide. That is, the meridional radiation of wave activity is stronger if the transition of PV across the tropopause is smoothed resulting in a waveguide that is less effective at trapping wave activity in the meridional direction.

Gray et al. (2014) suggested that both of the observed systematic model errors are dependent on model resolution, with lower resolution resulting in both a smoother isentropic gradient of PV at the tropopause and a larger reduction in ridge amplitude with lead time. As such, it can be expected that global climate models, with typical resolutions currently 5-20 times coarser than the operational NWP models, will exhibit even stronger biases. Indeed, long-standing climate model biases are that mid-latitude jet streams are too zonal, there is too weak jet stream variability, and an underestimation of the magnitude of large scale Rossby wave features including blocking. All these processes are

expected to be sensitive to the representation of Rossby waves in the models.

In a similar style to Harvey et al. (2016), the problem is here stripped back to its simplest relevant form using the single-layer quasi-geostrophic shallow water (QGSW) model. This model, together with some theoretical results regarding pseudo-momentum wave activity, are described in Section 2. The numerical scheme used to integrate the QGSW model is summarised in Section 3.

Two related model setups are then examined. First, in Section 4, the evolution of Rossby waves on a smooth PV step under nearly-inviscid dynamics is studied by varying the width of the PV transition region in the initial condition. The idea is to mimic the response of a Rossby wave following the fast reduction in the isentropic gradient of PV at the tropopause observed in the NWP models. The simulations show that smoothing the PV transition does result in a subsequent transient reduction in the amplitude of Rossby waves. The mechanism causing the amplitude reduction is explained in terms of the absorption of wave activity by the critical layers on the flanks of the jet, and a method for quantitatively predicting the magnitude of the reduction is presented. Second, in Section 5, the potential role of diffusion in the amplitude reduction is examined. Explicit diffusion is applied to a Rossby wave on an initially sharp PV step to mimic the continual smoothing of the PV gradient produced in model forecasts. A subsequent reduction of wave amplitude is observed via the nonlinear dynamics. Whilst a slow reduction in the large-scale wave amplitude could be expected from the direct effect of the diffusion at the lengthscale of the wave, it is shown that in reality the advective dynamics combines with the diffusion to produce a much faster damping of the large scale wave. The main conclusions are presented in Section 6.

2 Model Equations and Wave Activity Diagnostics

2.1 Quasi-Geostrophic Shallow Water Equations

The quasi-geostrophic shallow water (QGSW) model (e.g., Vallis, 2006) represents the large-scale dynamics of a single-layer fluid at small Rossby numbers. It is commonly used as a model of large-scale atmospheric motions as it incorporates the effects of both rotation and stratification in a simple fashion. The quasi-geostrophic PV q is related to the geostrophic streamfunction ψ via

$$q = f_0 + \nabla^2\psi - \frac{\psi}{L_R^2}, \quad (1)$$

where f_0 is the Coriolis parameter (here assumed constant) and the Rossby radius of deformation is $L_R = \sqrt{gH}/f_0$, where g is the acceleration due to gravity and H the average layer depth. The full depth of the fluid layer is, to QG accuracy, $h = H(1 + \psi/f_0L_R^2)$ and the horizontal wind is related to the streamfunction via $(u, v) = (-\psi_y, \psi_x)$, where $\mathbf{x} = (x, y)$ are the zonal and meridional coordinates respectively.

The PV evolution equation including a general non-conservative term S is

$$\frac{Dq}{Dt} = S \equiv \nabla \cdot \mathbf{F} \quad (2)$$

where D/Dt represents horizontal advection by the geostrophic wind. The focus here is on non-conservation of PV by dissipative processes and as such S is assumed to take the form of a divergence of a flux \mathbf{F} (as argued by Haynes & McIntyre (1987)).

Rossby waves can exist in this model anywhere there is a coherent gradient of q against which the Rossby wave restoring mechanism can act. Two archetypal linear solutions are for a uniform PV gradient and a narrow PV step (e.g. Hoskins & James, 2014). A uniform PV gradient is achieved on an f -plane by a constant zonal flow $u = U_0$ for which $q = f_0 + \hat{\beta}y$ where $\hat{\beta} = U_0/L_R^2$. Meridional displacements of PV contours of the form $\eta(x, y) = y + \eta_0 \exp(i(kx + ly - \omega t))$ are then a solution to (1) provided $c \equiv \omega/k = U_0 - \hat{\beta}L_R/\kappa^2$ where $\kappa = \sqrt{1 + (k^2 + l^2)L_R^2}$ is the effective wavenumber. For an infinitely narrow PV step $q = \mathcal{H}(y)\Delta q$ (here $\mathcal{H}(y)$ is the Heaviside step function) there is only a single active PV contour and displacements of the form $\eta(x) = \eta_0 \exp(i(kx - \omega t))$ are a solution of the linearised version of (1) provided $c \equiv \omega/k = \Delta q L_R (1 - 1/\kappa)/2$ (and $l = 0$). The physical mechanism is the same in both cases, however waves on a uniform PV gradient can propagate both zonally and meridionally whereas a narrow PV step acts as a waveguide and the waves can propagate in the zonal direction only.

2.2 Wave Activity Diagnostics

In the following, the configuration of a PV step is used, but rather than an infinitely narrow step as described above, a smooth step is considered in which q increases from 0 to Δq over a relatively narrow region of width σ near $y = 0$. For simplicity, the domain is taken to be periodic in the x -direction and of width X . The mechanism proposed for the reduction of Rossby wave amplitudes with time is that filamentation on the flanks of the jet is enhanced when the width of the step is broadened, leading to a more lossy waveguide. In order to quantify this effect, use is made of pseudo-momentum wave activity diagnostics, and a brief derivation of the required results is now presented.

2.2.1 Conservation of Zonal Momentum

The total zonal momentum in the QGSW system is

$$\hat{M} = H \iint \left(u - \frac{y\psi}{L_R^2} \right) dA, \quad (3)$$

where the integrand is the depth-integrated absolute zonal momentum in the shallow water system, $(u - f_0 y)h$, evaluated to QG accuracy with the constant leading-order term neglected (e.g. Bühler, 2009). For convenience the scaled momentum variable $M = \hat{M}/HX$ will be used from now on. Providing yu vanishes as $y \rightarrow \infty$, (3) can be integrated by parts to obtain

$$M = \int_{-\infty}^{\infty} y\bar{q} dy, \quad (4)$$

which is known as Kelvin's impulse. Bars denote the zonal mean: $\bar{q}(y) = \int_0^X q dx/X$.

The time evolution of M is found using the zonal mean of (2):

$$\frac{\partial \bar{q}}{\partial t} + \frac{\partial \bar{v}\bar{q}}{\partial y} = \frac{\partial \bar{F}}{\partial y} \quad (5)$$

where F is the y -component of $\mathbf{F} = (E, F)$ (e.g. Bühler, 2009). Therefore the zonal mean PV is modified by both advective rearrangements of PV and dissipation, but on substituting (5) into the time derivative of (4), integrating by parts and using the Taylor identity $\bar{v}\bar{q} = -(\overline{uv})_y$, it can be shown that

$$\frac{dM}{dt} = - \int_{-\infty}^{\infty} \bar{F} dy. \quad (6)$$

Therefore M is conserved if the domain integral of F vanishes. This is true for inviscid flow, but also if $S = \nabla \cdot \mathbf{F}$ is any linear function of vorticity field. For instance, linear diffusion of relative vorticity is given by $S = \nu \nabla^4 \psi$ for which $\bar{F} = \nu \bar{\psi}_{yyy}$ and the RHS of (6) vanishes. In contrast, linear diffusion of the full PV field has $S = \nu \nabla^2 q$ for which $\bar{F} = \nu \bar{q}_y$ and the RHS of (6) only vanishes if $\bar{q}(\infty) = \bar{q}(-\infty)$. This is because the diffusion affects the mass field as well as the wind field. For the case considered here of a PV step of magnitude Δq , the total zonal momentum M then decreases at the constant rate $-\nu \Delta q$.

2.2.2 Modified Lagrangian Mean Reference State

For any PV distribution $q(x, y)$, the modified Lagrangian mean (MLM) state is defined as that function $q_0(Y)$ obtained by rearranging $q(x, y)$ to be zonally symmetric and monotonically increasing in y (McIntyre, 1980) (note that here the notation of Nakamura & Zhu (2010) is used whereby the symbol Y represents the meridional coordinate in MLM space). The rearrangement should be conservative in the sense that the area enclosed by any PV contour is unchanged. Its evolution can be expressed as an integral along PV contours of the full wavy state (Methven, 2003)

$$\frac{\partial q_0}{\partial t} = \frac{1}{X} \frac{\partial q_0}{\partial Y} \oint_{q=q_0(Y)} \frac{S}{|\nabla q|} dl, \quad (7)$$

or alternatively as a flux divergence in MLM space (Nakamura & Zhu, 2010),

$$\frac{\partial q_0}{\partial t} = \frac{\partial F_0}{\partial Y} \quad (8)$$

where

$$F_0(Y) = \frac{1}{X} \oint_{q=q_0(Y)} \mathbf{F} \cdot \mathbf{n} dl \quad (9)$$

is the net flux of PV across the contour $q = q_0(Y)$ due to non-conservative processes and $\mathbf{n} = \nabla q / |\nabla q|$ is the unit vector normal to PV contours. That the expressions (7) and (8) are equivalent can be seen by using the divergence theorem to convert (9) to an integral over the area $q < q_0(Y)$ and then transforming to MLM space with the change of variables $|\nabla q| dA = q_{0,Y} dl dY$.

Comparing (8) with (5) shows that whereas \bar{q} is modified by both advective rearrangements of PV and non-conservative processes, q_0 is only modified by the latter. Note that if the non-conservative PV flux \mathbf{F} is downgradient then $F_0(Y) \geq 0$ everywhere. For the case of linear diffusion of PV, (9) can be written in terms of an effective diffusivity (Nakamura, 1996).

The MLM PV field $q_0(Y)$ can be inverted using (1) to find the corresponding reference state streamfunction $\psi_0(Y)$ and zonal wind $u_0(Y)$, and the total zonal momentum of the reference state is given by (cf. (4))

$$M_0 = \int_{-\infty}^{\infty} Y q_0(Y) dY. \quad (10)$$

It can be shown that $M_0 \geq M$ for any PV distribution q (e.g. this result follows from the theorem in Section 5 of Wood & McIntyre, 2010). In addition, substituting (8) into the time derivative of (10) gives

$$\frac{dM_0}{dt} = - \int_{-\infty}^{\infty} F_0(Y) dY, \quad (11)$$

which should be compared with (6). If the non-conservative PV flux \mathbf{F} is downgradient then M_0 must reduce in time.

2.2.3 Pseudo-Momentum Wave Activity

Following the above arguments, the quantity

$$\mathcal{A} = M_0 - M \quad (12)$$

satisfies $\mathcal{A} \geq 0$, with equality only if the full PV and the MLM PV are equal. \mathcal{A} is the pseudo-momentum wave activity. It can also be shown that \mathcal{A} is quadratic in disturbance amplitude at small amplitude, as measured by the meridional displacement of PV contours (see below). An interpretation of (12) is that any disturbance to a zonally-symmetric monotonically-increasing PV field can be associated with a westward pseudo-momentum of magnitude \mathcal{A} .

The evolution of \mathcal{A} is found by combining (6) and (11):

$$\frac{d\mathcal{A}}{dt} = - \int_{-\infty}^{\infty} F_0(Y) - \bar{F}(Y) dY. \quad (13)$$

Insight into this equation can be obtained, following Nakamura & Zhu (2010), by noting that the integrand represents the difference between the non-conservative PV flux across two contours: one following the wavy PV contour $q = q_0(Y)$ (see (9)) and the other oriented zonally at $y = Y$ (definition of \bar{F}). These two contours can be used as a definition of ridges and troughs for each PV contour $q_0(Y)$: those regions north of $y = Y$ where $q < q_0(Y)$ are ridges and those regions south of $y = Y$ where $q > q_0(Y)$ are troughs. The schematic in Figure 1 of Nakamura & Zhu (2010) illustrates these definitions. Invoking the divergence theorem over these regions, the integrand of (13) can be written

$$F_0(Y) - \bar{F}(Y) = \iint_{\substack{q < q_0(Y) \\ y > Y}} S dA - \iint_{\substack{q > q_0(Y) \\ y < Y}} S dA \quad (14)$$

where the first integral is over ridges and the second is over troughs. Therefore if non-conservative processes act, on average, to increase the PV in ridges and decrease the PV in troughs then wave activity \mathcal{A} is destroyed and the difference between M_0 and M will decrease. The difference between the initial and final states satisfies

$$\Delta\mathcal{A} = \Delta M_0 - \Delta M \quad (15)$$

and for the case discussed above where M is conserved, the value of M_0 must decrease towards M and the loss of wave activity is directly related to a modification of the reference state via

$$\Delta\mathcal{A} = \Delta M_0 = \int_{-\infty}^{\infty} Y \Delta q_0(Y) dY. \quad (16)$$

The integral wave activity \mathcal{A} can usefully be thought of as being distributed in space in several different ways. Considering decompositions in the meridional direction only, so that

$$\mathcal{A} = \int_{-\infty}^{\infty} A(Y) dY, \quad (17)$$

one definition is to take the wave activity density $A(Y)$ to be

$$A(Y) = \frac{dq_0 \overline{\eta^2}}{dY} \frac{1}{2}, \quad (18)$$

where $\eta(x, Y)$ is the meridional displacement of the contour $q = q_0(Y)$. This expression satisfies (12), even for large amplitude disturbances (Dritschel, 1988). It shows explicitly how the wave activity is quadratic in wave amplitude, as measured by the meridional displacement of PV contours.

An arguably more natural definition of wave activity density is provided by Nakamura & Zhu (2010) in terms of area integrals of PV. Their definition, denoted $A_{\text{NZ}}(Y)$ here, is described in the Appendix together with a discussion of its relationship to $A(Y)$. The definition $A_{\text{NZ}}(Y)$ exhibits several favourable properties, notably local extensions to both (12) and (13), valid for finite amplitude disturbances, together with the above interpretation that non-conservative processes act as an exchange between the wave activity and the reference state PV profile (see Appendix). However, for the purposes of the present study the fact that $A(Y)$ explicitly decouples the reference state PV gradient from meridional displacements of PV contours turns out to be more useful. As such, focus is given to $A(Y)$ in the following but $A_{\text{NZ}}(Y)$ is also computed to allow comparison with the finite amplitude wave activity theory of Nakamura & Zhu (2010).

3 Numerical Model

The evolution equation (2) is integrated numerically in a square $[0, 1] \times [0, 1]$ doubly-periodic domain using the same pseudo-spectral semi-Lagrangian code as Harvey et al. (2016) (see also Harvey & Ambaum, 2011, for further details) and a resolution of 1024 grid points in both the x and y directions. No explicit diffusion is required due to the favourable stability properties of the semi-Lagrangian scheme, although an explicit linear diffusion is added for some of the simulations, as described below. The dominant numerical error arises from the interpolation employed at back trajectory start points. In the simulations presented here a bicubic interpolation scheme is used and the resulting numerical error is approximately equivalent to a weak ∇^4 dissipation (Harvey, 2011). Simulations with no explicit diffusion applied will be called ‘nearly-inviscid’ and, following the discussion at the end of Section 22.22.2.1, the total zonal momentum M can be expected to remain almost constant in these cases.

Simulating a step-like PV profile in a doubly-periodic domain can be problematic since a jump in PV is present at the top/bottom boundary of the domain. This issue is avoided here by decomposing the PV field as $q = y\Delta q/L + q'$, where L is the domain size and Δq the jump in PV, and using q' for both the advection and inversion operations. In effect, this approach is equivalent to simulating an infinite staircase of PV jumps in the y -direction, each carrying an identical Rossby wave disturbance (e.g. Dritschel & McIntyre, 2008).

Two sets of simulations are presented. In Section 4 nearly-inviscid simulations are performed ($S = 0$) for a range of wave-like initial conditions. These are generated by meridionally perturbing a sharp PV step and then smoothing the resulting field. The aim is to mimic the reduced PV gradient across the tropopause exhibited by the NWP models. The shape of the perturbation used is the steadily-propagating weakly-nonlinear solution for a sharp PV step derived by Esler (2004). It consists of a superposition of the fundamental harmonic of wavenumber k and a first-order correction of wavenumber $3k$.

This correction sharpens the sinusoid slightly, making the perturbation more saw-like, resulting in a disturbance which (almost) propagates with a constant shape in the sharp step limit. However, for the cases shown here this correction has little effect on the results. The smoothing used is a 2D Gaussian filter, given by

$$q(\mathbf{x}) = \frac{1}{2\pi\sigma^2} \iint q_{\text{sharp}}(\mathbf{x}') \exp\left(\frac{-|\mathbf{x} - \mathbf{x}'|^2}{2\sigma^2}\right) d^2\mathbf{x}', \quad (19)$$

where σ is a lengthscale of the smoothing. Note that this smoothing is equivalent to applying a linear diffusion to the PV field for a time $t = \sigma^2/2\nu$. In Section 5 simulations are performed with explicit diffusion added ($S = \nu\nabla^2q$) and the initial condition used is the sharp PV step, perturbed as above but with no smoothing applied.

4 Decay of waves on a smooth PV step under nearly-inviscid dynamics

4.1 An Example Simulation

Figure 1 shows an illustration of the problem addressed here: the evolution of a Rossby wave on a smooth PV step. Panel (a) shows the initial condition and panels (b) and (c) show snapshots at non-dimensional times $t = 80$ and $t = 1000$ of the subsequent nearly inviscid evolution. This example simulation has a Rossby radius $L_R = 1/4\pi$, a basic state smoothing lengthscale $\sigma = 0.7L_R$, an initial disturbance amplitude $a = L_R$ and wavenumber $k = 1/L_R$, meaning the computational domain contains two wave lengths. The jump in PV across the domain is $\Delta q = 1$. In order to interpret the timescale of the evolution, the dimensional frequency scale $\Delta q^* = 2 \times 10^{-4} \text{ s}^{-1}$ suggested by Swanson (2001) is employed, meaning one time unit corresponds to $(\Delta q^*)^{-1} \approx 1.5$ hours and the non-dimensional times $t = 80$ and $t = 1000$ correspond roughly to 5 days and 60 days respectively.

As the simulation proceeds the Rossby wave propagates towards the right. However, the PV field quickly becomes distorted as PV on the flanks of the jet is advected around the eddies that make up the ridges and troughs. These eddies represent the critical layers of the Rossby wave. Critical layers are regions where the phase speed of the wave equals the background jet speed (Haynes, 2003). As a result, the streamlines of the flow form closed loops when viewed in the frame of reference moving with the wave (see Figure 5). Figure 1b shows time $t = 80$ which corresponds to roughly half the time for advection around the eddies. By the time $t = 1000$ (Figure 1c) the anomalous PV has recirculated several times and become mixed by the combined effects of stirring to small scales and the weak implicit diffusion inherent in the numerical scheme. In contrast, in a simulation run with a sharp PV step (not shown) the wave disturbance propagates towards the right with no noticeable distortion of the PV contours.

As noted above, the total zonal momentum of the flow M is expected to be approximately conserved during the simulation (see (6) and subsequent discussion). In contrast, the mixing of PV on the flanks of the jet will act to reduce the total zonal momentum of the MLM state M_0 (via (11)) and therefore also the pseudo-momentum \mathcal{A} (via (16)). Figure 2a shows timeseries of all three quantities and confirms this is the case. The changes in all three quantities between the initial time and the two snapshots in Figure 1 are shown in Table 1.

Of interest here is the evolution of the amplitude of the large-scale Rossby wave. To quantify this, Figure 2b shows the primary wave amplitude, defined as the root mean square displacement of the central PV contour: $\sqrt{\overline{\eta^2}(Y=0)}$. The primary wave amplitude exhibits a decrease by around 30% over the course of the simulation, but superimposed on the decrease is an oscillation with a period of around 170 time units. The timing of this pulsing of wave amplitude is associated with the advective recirculation of anomalous PV around the critical layers described above. In conjunction with the pulsing of wave amplitude, the maximum of the zonal mean zonal wind (Figure 2c) exhibits an oscillation with the same frequency but the opposite phase: when the wave amplitude is minimum, the zonal mean jet is strongest. Also shown in Figure 2c is the maximum of the MLM reference state jet which remains almost constant during the simulation.

In summary, smoothing the initial PV profile has resulted in a transient decrease in primary wave amplitude. The aim of the following sections is to quantify this process in order to assess whether it can be expected to play a role in the reduction in Rossby wave amplitude observed in NWP forecasts. In the following subsection the link to the recirculation of anomalous PV around the critical layers is made more precise, using the terminology of Killworth & McIntyre (1985), in terms of the absorption and over-reflection of wave activity by the critical layers. This explanation is then used in Section 4.3 to construct an estimate for the magnitude of the reduction of primary wave amplitude expected for a given amount of smoothing.

4.2 The Example Simulation In More Detail

To explore the link between the redistribution of PV on the flanks of the jet and the reduction in primary wave amplitude, Figure 3 shows meridional profiles of various diagnostics from the example simulation at time $t = 0$ (solid lines) and at times $t = 80$ (dashed lines, upper panels) and $t = 1000$ (dashed lines, lower panels). These are the same times as shown in Figure 1 and Table 1.

At the initial time, the MLM PV profile represents a smooth transition from low to high values (Figure 3a). The gradient of MLM PV is peaked at $Y = 0$ (Figure 3b), whereas the value of $\overline{\eta^2}$ is more constant across the domain, varying from values of 1×10^{-3} on the jet flanks to 2×10^{-3} in the jet core (Figure 3c, solid line). The wave activity density $A(Y)$ (see (18)) is the product of the two, and as such its shape is dominated by the strong meridional variation of the MLM PV gradient (Figure 3d, solid line). The wave activity density $A_{\text{NZ}}(Y)$ (see 21) is almost indistinguishable from A for the initial condition PV distribution (Figure 3d, solid grey line).

By the time $t = 80$ the weak implicit hyperdiffusion has had very little impact on the MLM PV profile or its gradient (Figures 3a, b, dashed lines). Consistently, there has been very little modification of the total wave activity \mathcal{A} (Table 1). However, there has been a marked redistribution of wave activity density within the domain. The advection of the PV filaments to the outer edges of the critical layers has resulted in an increase of $\overline{\eta^2}$ there (Figure 3c, dashed line). Because the MLM PV profile is unchanged, the changes in $\overline{\eta^2}$ are exactly mirrored by changes in $A(Y)$ (Figure 3d, dashed line). There are also qualitatively similar changes in $A_{\text{NZ}}(Y)$, although the relation to $\overline{\eta^2}$ is more complex. In the terminology of Killworth & McIntyre (1985), the initial evolution of the critical layer has acted to absorb wave activity from the surrounding fluid. Since the total wave activity \mathcal{A} is conserved, the increase in wave activity density A on the jet flanks is exactly compensated by a reduction in $\overline{\eta^2}$ in the jet core (Figure 2b). Note that the reduction in

primary wave amplitude described above is evident as this decrease in $\overline{\eta^2}$ at $Y = 0$. If this reduction in wave amplitude had not occurred then the total momentum of the flow could not have been conserved.

During the subsequent evolution, wave activity density repeatedly oscillates between the jet core and the critical layer, as shown in Figures 4b and c. By the time $t = 1000$ there has been some dissipative loss of M_0 due to the implicit dissipation present in the numerical scheme (Table 1). This is manifested as a flattening of the q_0 profile on the jet flanks (Figures 3e and 4a), and is associated with the loss of an almost equal amount of wave activity from the flow, consistent with (16) (Table 1). The small difference between them is accounted for by the change in M which arises as a result of numerical inaccuracies. As a result of the flattening of q_0 , there are spikes in the MLM PV gradient profile on each edge of the mixing region, which are inherited by the wave activity density $A(Y)$, but not by $A_{\text{NZ}}(Y)$. The reduction of total wave activity between $t = 80$ and $t = 1000$ is manifested predominantly as a reduction of $\overline{\eta^2}$ on the jet flanks (Figure 3g), consistent with the dissipation of small-scale features occurring there.

In summary, at both times examined there is a smaller primary wave amplitude than in the initial condition. At time $t = 80$ the reduction is associated with an adiabatic absorption of wave activity into the critical layers. This represents a reversible process associated with a conservative rearrangement of PV during which the total wave activity \mathcal{A} is conserved. At time $t = 1000$ the reduction is due to a combination of the adiabatic absorption by the critical layer and a dissipative modification of the MLM PV field due to mixing. This latter process represents an irreversible exchange of momentum between \mathcal{A} and background state M_0 via (16).

4.3 Quantitative Prediction of the Reduction in Primary Wave Amplitude

Assuming the change in primary wave amplitude is not too large, the streamfunction of the flow, viewed in the frame of reference of the primary wave, will remain approximately constant during the integration. As such, the PV anomalies that are advected around the closed streamlines of the critical layers can be expected to behave, at leading order, like passive tracers. This observation is now used to construct estimates for the reduction in primary wave amplitude resulting for given amount of smoothing.

Rhines & Young (1983) studied the mixing of passive tracers by advection and diffusion within steady, closed streamlines and showed that such mixing acts to homogenise the tracer throughout the closed-streamline region. However, this process occurs in three stages. Initially, the tracer is advected around the closed streamlines on the eddy turnover timescale T_e . During the second stage the diffusion combined with the cross-flow shear acts to homogenise the tracer around the streamlines on a timescale of T_a . During the final stage the cross-flow variations in tracer are then reduced by diffusion on a timescale of T_d . Although in the numerical simulations presented here the mixing is achieved by the ∇^4 -like numerical error, rather than a ∇^2 diffusion, a similar process is expected to apply. In particular, the second stage is expected to be slower than the eddy turnover time but faster than the final stage: $T_e \ll T_a \ll T_d$.

This analysis is consistent with the illustration shown in Figures 1 and 2. The eddy turnover time T_e is evident as the fast pulses in primary wave amplitude, whereas the timescale for the along-streamline homogenisation T_a is evident in its gradual reduction (Figure 2b). The final stage of homogenisation whereby PV becomes uniform throughout

the eddy is not yet achieved by the end of the simulation, as is apparent in Figure 1c.

Motivated by this analysis, two simple approximations of the PV field at specific stages of the evolution are now constructed. In both cases the initial PV field is artificially rearranged around streamlines in the frame of reference of the wave, as described below. Figure 5a shows the initial condition PV field and the streamlines in the frame of reference of the wave for the example simulation. There are closed streamlines on both flanks of the jet, representing the critical layer circulation around the troughs and ridges. The phase speed of the wave c has here been estimated by minimising the variation of the streamfunction along the $q = 0$ contour, and the streamfunction in this frame of reference is given by $\psi_{\text{shift}} = \psi + cy$.

For the first PV rearrangement, q_{con} , PV is conservatively rearranged around each closed streamline of the initial condition so that their PV values decrease with y . The aim is to approximate the initial advection of high PV values to the outer edges of the critical layers at time $t = 80$ (Figure 1b). The resulting PV field is shown in Figure 5b. For the second PV rearrangement, q_{mix} , PV values are mixed along streamlines so that all points along each streamline take the same PV value equal to the area-weighted mean PV along the streamline in the initial condition. The aim is to mimic the PV distribution at time $t = 1000$ (Figure 1c) after which the PV has become homogenised along streamlines. The resulting PV field is shown in Figure 5c.

The hypothesis is that neither q_{con} or q_{mix} are physically achievable states since neither conserve the total momentum M . In fact, both are expected to have smaller M than the initial condition. In practice, the full simulation cannot lose momentum, and instead the momentum deficit must be extracted from the reservoir of pseudo-momentum associated with the primary wave.

To test this hypothesis, Figure 6 shows the meridional profile diagnostics for q_{con} or q_{mix} and should be compared with the results from the full simulation in Figure 3. The similarity between the artificially-generated profiles and the full simulation is remarkable. Comparing first q_{con} with the full simulation at time $t = 80$, both have profiles of MLM PV and its gradient almost unchanged from the initial condition (panels a and b). There are also similar large increases in $\overline{\eta^2}$ and A on the jet flanks (panels c and d). Crucially, however, q_{con} does not exhibit the compensating reductions in $\overline{\eta^2}$ and A in the jet core observed in the full simulation. As such, there is a net loss of total momentum M between the initial condition and q_{con} (see Table 1). Likewise, the MLM PV and its gradient are almost indistinguishable between q_{mix} and the full simulation at time $t = 1000$ (panels e and f). The flattening of the MLM PV profile on the jet flanks and the associated spikes in its gradient are well captured by q_{mix} , and $\overline{\eta^2}$ and A show similar increases in the jet flank region (panels h and i). Again, the reduction in the jet core observed in the full simulation is not present and as a result there is a net loss of total momentum M associated with the artificial mixing (Table 1).

To formulate predictions for the reduction of primary wave amplitude at these two stages of the evolution, it is assumed that the meridional displacement of PV contours within the jet core region reduce by a uniform factor λ from $\eta(x, y)$ to $\lambda\eta(x, y)$. Here the jet core is defined as that region between the spikes in the MLM PV gradient of the rearranged PV distributions: $|Y| < Y_{\text{spike}}$. In practice, Figures 3c and g show that the reduction is not precisely uniform, but this assumption provides a reasonable estimate. This reduction in amplitude corresponds to a reduction of wave activity density from A to $\lambda^2 A$ (see 18). Using (12) to equate the net loss of wave activity to the deficit of total

momentum M arising from the PV rearrangement gives an expression for λ :

$$(1 - \lambda^2) \int_{-Y_{\text{spike}}}^{Y_{\text{spike}}} A(Y) dY = \Delta M_R, \quad (20)$$

where ΔM_R is the momentum deficit from either performing the conservative rearrangement around closed streamlines, $\Delta M_R = M_{\text{con}} - M$, or the non-conservative mixing along streamlines, $\Delta M_R = M_{\text{mix}} - M$, where M is calculated using (4). In either case, a value for the amplitude reduction factor of the primary wave, λ , is obtained from knowledge of the initial wave activity distribution A (defined by (18)), the loss of total zonal momentum resulting from the artificial PV rearrangement ΔM , and the width of the mixing zonal as specified by Y_{spike} .

To test the prediction (20), a suite of simulations has been performed, identical to the example simulation except covering a range of initial smoothing length scales: $\sigma = 0.1L_R$ to $\sigma = 1.2L_R$. For each simulation, the primary wave amplitude reduction is computed both at the time of its first minimum, corresponding to half an eddy turnover time, and as an average over the times $t = 800 - 1200$, representing the mean amplitude at the end of the simulation (Figure 7, black symbols). Both of these quantities decrease monotonically with the smoothing width, with the amplitude at half an eddy turnover time always smaller than the final amplitude.

Also shown in Figure 7 (grey symbols) are the estimates of λ from (20), for both q_{con} or q_{mix} . For $\sigma < 0.7L_R$ both estimates provide a reasonable quantitative agreement with the full simulations, especially given the level of approximation involved. Beyond $\sigma = 0.7L_R$ the estimate using q_{con} for the amplitude at half an eddy turnover time becomes too small. Beyond $\sigma = 1.0L_R$ the estimate using q_{mix} for the mean amplitude at the end of the simulation also fails. The breakdown of the theory at large smoothing widths can be anticipated, since in those cases the reduction in amplitude is large so the assumption of steady streamlines in the moving frame of reference is not justified. However, the aim of this exercise is to understand the mechanism causing the reduction of Rossby wave amplitude when the smoothing width is varied, and the fact that the estimates from (7) agree quantitatively with the full simulations for moderate σ values provides strong evidence that it is the absorption of wave activity by the critical layers that is responsible.

4.4 Comparison with Operational Weather Forecast Results

A key result of the previous section was the illustration that a reduction in Rossby wave amplitude can be expected to follow a fast smoothing of the isentropic gradient of PV at the tropopause, as a direct result of the adiabatic rearrangement of PV on the flanks of the jet. In order to assess the potential relevance of this process in operational NWP forecasts, both the timescale of the process and the potential magnitude of its impact are now discussed.

Whilst the arguments above discussed both the timescale for the initial amplitude reduction T_e and the longer timescale for the homogenisation of PV along closed streamlines T_a , it is clear from Figure 1b that the initial impact on the primary wave amplitude is felt most strongly over the short advective timescale T_e . In practice, this represents the circulation of air around the critical layers either side of the jet, typically associated with large amplitude Rossby waves and blocking, and as such will depend on the synoptic situation but can be expected to take around 2-5 days. In terms of magnitude, Figure 7 shows that the impact on primary wave amplitude varies quadratically with the smoothing width.

Considering the typical values quoted in Harvey et al. (2016) of $\sigma = 0.44L_R$ for the width of the PV transition in a typical analysis state and $\sigma = 0.54L_R$ for a typical 5-day forecast state, values for the amplitude reduction read off of Figure 7 are 0.86 and 0.78 respectively. Therefore the impact of the isentropic gradient error on the primary wave amplitude after 5 days is $O(10\%)$. Taken together, both the timescale and magnitude of the process, as estimated from the simple single-layer QGSW model, appear to agree remarkably well with the results of Gray et al. (2014). For instance, their Figure 5 shows that both of the two NWP models which show a consistent picture between different winter seasons exhibit a reduction in ridge area of $O(10\%)$ over a period of 5 days.

5 The Role of Diffusion in Affecting the Amplitude Reduction

The explanation of a reduction in Rossby wave amplitude associated with a smoothing of the isentropic transition of PV at the tropopause provides an interesting interpretation of the impact of diffusion in atmospheric models more generally. Diffusion, used explicitly or implicitly in NWP models to make the numerics stable, acts preferentially at small scales. As such, the direct effect on large-scale Rossby waves can be expected to be small. However, the effect of diffusion across the strong tropopause gradient may be substantial and the result of diffusion of PV near the jet is to smooth the PV profile. If the subsequent evolution is such that the anomalous PV due to the smoothing is advected as in Figure 1b, then the nonlinear dynamics provides a route by which diffusion at small scales can act to damp the large-scale waves via additional filamentation.

To explore this possibility further numerical simulations are performed. Rather than vary the width of the initial condition PV profile in the nearly-inviscid model, as was done above, an initial PV distribution with a very narrow PV step is used in simulations using a range of diffusion parameters. To pick apart the impact of the diffusion acting directly on the large-scale wave from the critical layer dynamics on the jet flanks, two sets of simulations are performed. The first uses the full model with diffusion switched on, and the other has diffusion switched on but advection switched off. That is, the advecting velocity fields set to zero at each time step.

Figure 8 shows the initial condition PV distribution used in all of these simulations (panel a) together with the final states from one example simulation using the full model (panel b) and the corresponding simulation with advection switched off (panel c). The mixing of PV around the closed streamlines of the critical layers is evident in the full model, but not when advection is switched off. In addition, the greater reduction of primary wave amplitude in the former case is clear. Figure 9 shows the timeseries diagnostics for these two simulations. As expected from the discussion in Section 22.22.2.1, the diffusion acts to reduce the total momentum M linearly in time, at the same rate in both simulations (panel a, solid lines). The reduction of M_0 is faster than the reduction of M in both simulations, indicating a decay of wave activity with time via (12) (panel a, dashed lines). The decay of wave activity in the simulation with advection switched off occurs due to the linear dissipation of PV anomalies by the diffusion. However, the decay of wave activity when advection is switched on is much faster, highlighting the impact of the nonlinear advection on the decay of Rossby waves. Consistently, the reduction in primary wave amplitude is much faster when advection is switched on (panel b). Finally, whilst the MLM zonal mean wind maximum decreases in both simulations, the zonal

mean wind maximum exhibits, counter-intuitively, a transient increase when both advection and diffusion are acting (panel c). This represents the process whereby absorption of wave activity by the critical layers acts to reduce the primary wave amplitude and thus straighten the jet and increase the zonal mean wind, initially faster than the diffusion acts to damp the local wind speeds. This process could potentially act to hide a model bias whereby an accurate zonal mean wind field may camouflage the competing influences of excessive diffusion, for a short time at least.

In order to summarise the impact of the nonlinear processes in enhancing the Rossby wave reduction in all simulations, Figure 10 shows the instantaneous decay rates of the primary wave amplitude, for both the simulations with and without advection switched on. Typically, after an initial adjustment there is a period with an almost constant decay rate with time. Over the range of diffusion parameters tested, the decay of the primary wave amplitude typically occurs at a rate 2–4 times faster when advection is switched on than when advection is switched off. Therefore the impact of diffusion in a numerical simulation may be expected to damp the large-scale waves up to 4 times faster than a simpler argument based on diffusive damping of modes would suggest. The factors influencing this number have not been investigated here, but presumably simulations with different amplitude, wavelength and shape of Rossby waves may have different amplification factors.

6 Conclusions

This study explores a mechanism by which the amplitude of Rossby waves may reduce with lead time in numerical models. NWP models are known to exhibit a systematic bias in which the amplitudes of Rossby waves reduce, on average, during the first 5 days of forecasts (Gray et al., 2014). Previous studies have suggested that the representation of diabatic processes in numerical models may contribute directly to this bias via the associated mass flux into upper-tropospheric ridges. Here an alternative candidate is explored whereby the isentropic gradient of PV at the tropopause plays a key role. A too smooth PV gradient at the tropopause is expected to result in a reduction in Rossby wave amplitudes.

Using a single-layer quasi-geostrophic model to understand the mechanism it is shown that a too smooth transition at the tropopause from low PV tropospheric air to high PV stratospheric air results in a more lossy waveguide. Rossby wave activity disperses meridionally and is absorbed by the critical layers on the flanks of the jet, leaving behind a smaller-amplitude meandering of the jet core. The relevance of this mechanism, at least for the simple model, is demonstrated by using it to construct a quantitative prediction of the magnitude of the amplitude reduction, valid in the relevant regime for NWP whereby the $\sigma < 0.7L_R$. Based on rough order-of-magnitude estimates, this mechanism seems likely to play a role in NWP and climate models.

An alternative view on the meridional dispersion of Rossby wave activity of a smoothed PV front is provided by linear wave theory. In particular, Held (1985) shows that any linear perturbation on a zonal shear flow can be uniquely partitioned into discrete modes and a continuum of singular modes (see also Held & Phillips (1987)). The continuum modes typically decay exponentially in time due to the background shear, leaving the discrete modes to dominate the long-time behaviour. For the problem of a smoothed PV front, Harvey et al. (2016) derive analytic expressions for the discrete mode of a slightly-smoothed PV front, based on an asymptotic expansion for small smoothing widths. In principle this discrete mode structure could be used to estimate the reduction in wave

amplitude according to linear dynamics. We did not explore this argument here, however, because it does not provide a distinction between the short eddy-turnover time and the long PV mixing timescales as the new method does. In addition, the PV rearrangement argument presented is more intuitive than interpreting the decay of the continuous spectrum modes. Exploring the relationship between the prediction from linear theory and the prediction from the PV mixing argument presented here may provide further insight into the problem.

The mechanism explored in this paper is characterised by the advective rearrangement of PV around critical layers. As such, it is nonlinear and adiabatic in nature. However, the initial cause of the enhanced PV fluxes is the reduction in PV gradient at the tropopause in the early stages of global forecasts (Gray et al., 2014). Possible reasons for this include the representation of diabatic heating near the tropopause, particularly radiative cooling (Chagnon et al., 2013; Saffin et al., 2017), and the use of (implicit or explicit) diffusion in the models. Insight into the latter case is gained by applying diffusion to Rossby waves on a sharp PV step in the single-layer model. It is shown that the combined impact of the diffusion acting on the small scales of the PV step and the adiabatic rearrangement of the resulting PV anomalies results in a reduction of Rossby wave amplitude that is 2–4 times faster than would result from the diffusion acting alone. This illustrates a mechanism whereby the overly-diffusive nature of many NWP and climate models may have a damping effect on the large-scale wave amplitudes which is substantially larger than a simple estimate based on the linear diffusive damping of modes would suggest.

Since the mechanism involves the resolved flow on the flanks of the jet, it is expected that its presence in operational NWP models can be detected by an analysis of isentropic PV fluxes. In particular, the increase in wave activity density on the jet flanks in Figure 3 is associated with the Eliassen-Palm fluxes via (22). Future work will investigate the PV fluxes in NWP forecasts to understand the extent that this mechanism occurs in current state of the art models.

Acknowledgments

The authors would like to thank the three anonymous reviewers for their valuable comments and suggestions to improve the manuscript. This work was partially-supported by the Natural Environment Research Council [grant number NE/M014932/1].

A Alternative definition of wave activity density

Equation (18) defines the formulation of wave activity density used in this study. An alternative definition is provided by Nakamura & Zhu (2010) in terms of area integrals of PV. Based on their Equation (18), their version can be expressed as

$$A_{\text{NZ}}(Y) = \int_{-\infty}^Y (\bar{q} - q_0) dY, \quad (21)$$

provided there is no disturbance at $y \rightarrow -\infty$.

This expression satisfies (12) for any disturbance, as is readily seen by integrating by parts. Its evolution, found by combining (5) and (8), is given by

$$\frac{\partial A_{\text{NZ}}}{\partial t} + \overline{vq} = \bar{F} - F_0 \quad (22)$$

meaning A_{NZ} can be fluxed around the domain during advective rearrangements of PV and it can be locally modified by non-conservative processes in ridges and troughs via (14). This equation provides a natural local extension to the evolution Equation (13) for the total wave activity \mathcal{A} and its interpretation described below equation (13). There is no such simple relationship for A . Furthermore, taking the second derivative of the definition (21) gives

$$\frac{\partial^2 A_{\text{NZ}}}{\partial Y^2} = \mathcal{L}(\bar{u}) - \mathcal{L}(u_0), \quad (23)$$

where

$$\mathcal{L}(\psi) = \nabla^2 \psi - \frac{\psi}{L_R^2} \quad (24)$$

is the linear PV operator. Equation (23) provides a natural local extension of (12) whereby wave activity density is directly related to the difference between the zonal mean flow and the MLM state. Again, there is no such simple relationship for A . Whilst A and A_{NZ} are different in general, they agree in the limit of small amplitude disturbances provided $q_0(Y)$ is sufficiently smooth (Nakamura & Zhu, 2010). As such, for small amplitude disturbances both quantities satisfy the two properties (22) and (23), but these are only strictly valid for large amplitude disturbances for A_{NZ} .

The difference between A and A_{NZ} when $q_0(Y)$ is not smooth can be understood by considering the extreme case of a single sharp PV step, perturbed to the position $y = \eta(x)$. The expression (18) takes the form of a δ -function which is zero everywhere except at the latitude of the step where its amplitude is infinite and proportional to $\int \eta^2 dx$. In contrast, the expression (21) is non-zero over all latitudes in the region $\min \eta < y < \max \eta$, where it is finite and its maximum value is and proportional to $\int \eta dx$. The expression (18) effectively loads the wave activity onto those *equivalent latitudes* of the MLM reference state whose contours are perturbed to produce the full PV field, whereas the expression (21) loads the wave activity onto those *physical latitudes* of the full PV state at which there are PV anomalies present.

Since the arguments presented in section 4 directly concern the meridional displacement of PV contours, it requires the use of the wave activity density A from Equation (18). However, given the intuitive local properties of A_{NZ} outlined above, this quantity is also presented in Figures 3, 4 and 6 to allow a comparison between the two diagnostics.

References

- Bühler, O. 2009 *Waves and mean flows*. Cambridge University Press.
- Chagnon, J. M., Gray, S. L. & Methven, J. 2013 Diabatic processes modifying potential vorticity in a North Atlantic cyclone. *Q. J. Roy. Meteor. Soc.* **139**, pp. 1270–1282.
- Dritschel, D. G. 1988 Nonlinear stability bounds for inviscid, two-dimensional, parallel or circular flows with monotonic vorticity, and the analogous three-dimensional quasi-geostrophic flows. *J. Fluid Mech.* **191**, pp. 575–581.
- Dritschel, D. G. & McIntyre, M. E. 2008 Multiple jets as PV staircases: the Phillips effect and the resilience of eddy-transport barriers. *J. Atmos. Sci.* .
- Esler, J. G. 2004 Benjamin–Feir instability of Rossby waves on a jet. *Q. J. Roy. Meteor. Soc.* **130**, pp. 1611–1630.

- Grams, C. M. & Archambault, H. M. 2016 The key role of diabatic outflow in amplifying the midlatitude flow: A representative case study of weather systems surrounding western North Pacific extratropical transition. *Mon. Wea. Rev.* **144**, pp. 3847–3869.
- Grams, C. M., Wernli, H., Böttcher, M., Čampa, J., Corsmeier, U., Jones, S. C., Keller, J. H., Lenz, C.-J. & Wiegand, L. 2011 The key role of diabatic processes in modifying the upper-tropospheric wave guide: A North Atlantic case-study. *Q. J. Roy. Meteor. Soc.* **137**, pp. 2174–2193.
- Gray, S. L., Dunning, C. M., Methven, J., Masato, G. & Chagnon, J. M. 2014 Systematic model forecast error in Rossby wave structure. *Geophys. Res. Lett.* **41**, pp. 2979–2987.
- Harvey, B. J. 2011 *Surface effects in quasi-geostrophic dynamics*. Ph.D. thesis, University of Reading.
- Harvey, B. J. & Ambaum, M. H. P. 2011 Perturbed Rankine vortices in surface quasi-geostrophic dynamics. *Geophys. & Astro. Fluid Dyn.* **105**, pp. 377–391.
- Harvey, B. J., Methven, J. & Ambaum, M. H. P. 2016 Rossby wave propagation on potential vorticity fronts with finite width. *J. Fluid Mech.* **794**, pp. 775–797.
- Haynes, P. H. 2003 Critical layers. In *Encyclopedia of Atmospheric Sciences*, volume 2. pp. 582–589.
- Haynes, P. H. & McIntyre, M. E. 1987 On the evolution of vorticity and potential vorticity in the presence of diabatic heating and frictional or other forces. *J. Atmos. Sci.* **44**, pp. 828–841.
- Held, I. M. 1985 Pseudomomentum and the orthogonality of modes in shear flows. *J. Atmos. Sci.* **42**, pp. 2280–2288.
- Held, I. M. & Phillips, P. J. 1987 Linear and nonlinear barotropic decay on the sphere. *J. Atmos. Sci.* **44**, pp. 200–207.
- Hoskins, B. J. & James, I. N. 2014 *Fluid Dynamics of the Mid-Latitude Atmosphere*. Wiley and Sons.
- Hoskins, B. J., McIntyre, M. E. & Robertson, A. W. 1985 On the use and significance of isentropic potential vorticity maps. *Q. J. Roy. Meteor. Soc.* **111**, pp. 877–946.
- Killworth, P. D. & McIntyre, M. E. 1985 Do Rossby-wave critical layers absorb, reflect, or over-reflect? *J. Fluid Mech.* **161**, pp. 449–492.
- Madonna, E., Wernli, H., Joos, H. & Martius, O. 2014 Warm conveyor belts in the ERA-Interim dataset (1979–2010). Part I: Climatology and potential vorticity evolution. *J. Clim.* **27**, pp. 3–26.
- Martínez-Alvarado, O., Madonna, E., Gray, S. L. & Joos, H. 2016 A route to systematic error in forecasts of Rossby waves. *Q. J. Roy. Meteor. Soc.* **142**, pp. 196–210.
- McIntyre, M. E. 1980 Towards a Lagrangian-mean description of stratospheric circulations and chemical transports. *Phil. Trans. Roy. Soc. London* **A296**, pp. 129–148.

- Methven, J. 2003 The influence of PV inversion on polar-vortex dynamics and passive-tracer simulations in atmosphere-like regimes. *Q. J. Roy. Meteor. Soc.* **129**, pp. 1191–1215.
- Nakamura, N. 1996 Two-dimensional mixing, edge formation, and permeability diagnosed in an area coordinate. *J. Atmos. Sci.* **53**, pp. 1524–1537.
- Nakamura, N. & Zhu, D. 2010 Finite-amplitude wave activity and diffusive flux of potential vorticity in eddy-mean flow interaction. *J. Atmos. Sci.* **67**, pp. 2701–2716.
- Rhines, P. B. & Young, W. R. 1983 How rapidly is a passive scalar mixed within closed streamlines? *J. Fluid Mech.* **133**, pp. 133–145.
- Saffin, L., Gray, S. L., Methven, J. & Williams, K. D. 2017 Processes maintaining tropopause sharpness in numerical models. *J. Geophys. Res.* **122**, pp. 9611–9627.
- Schäfler, A., Craig, G., Wernli, H. & co authors 2018 The North Atlantic Waveguide and Downstream Impact Experiment. *Bull. Amer. Meteor. Soc.* .
- Swanson, K. L. 2001 Blocking as a local instability to zonally varying flows. *Q. J. Roy. Meteorol. Soc.* **127**, pp. 1341–1355.
- Vallis, G. K. 2006 *Atmospheric and Oceanic Fluid Dynamics*. Cambridge University Press.
- Wood, R. B. & McIntyre, M. E. 2010 A general theorem on angular-momentum changes due to potential vorticity mixing and on potential-energy changes due to buoyancy mixing. *J. Atmos. Sci.* **67**, pp. 1261–1274.

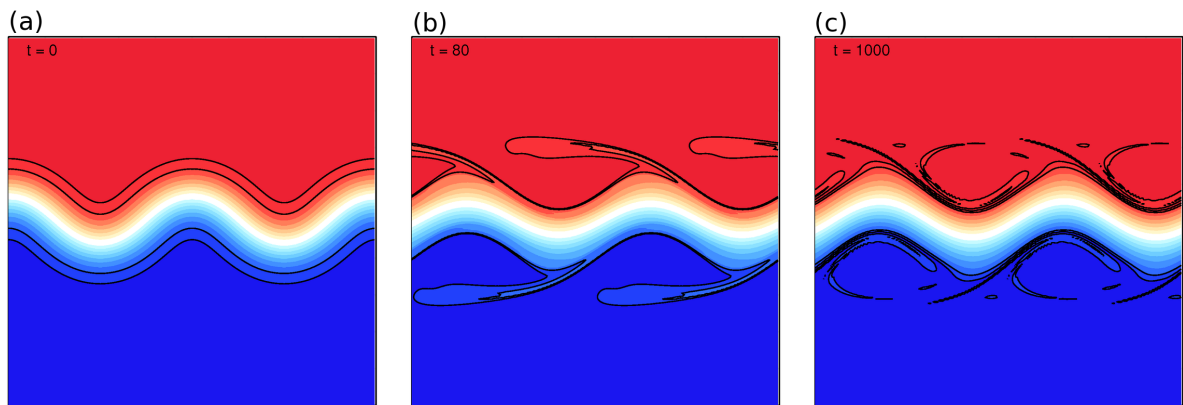


Figure 1: The PV field at times (a) $t=0$, (b) $t=80$, and (c) $t=1000$ from the illustrative simulation with wave amplitude $a = L_R$, wavenumber $k = 1/L_R$, and smoothing width $\sigma = 0.7L_R$. In each panel the two outermost contours are marked by solid lines for clarity. The full 1×1 model domain is shown. A movie of this simulation is provided in the supplementary material.

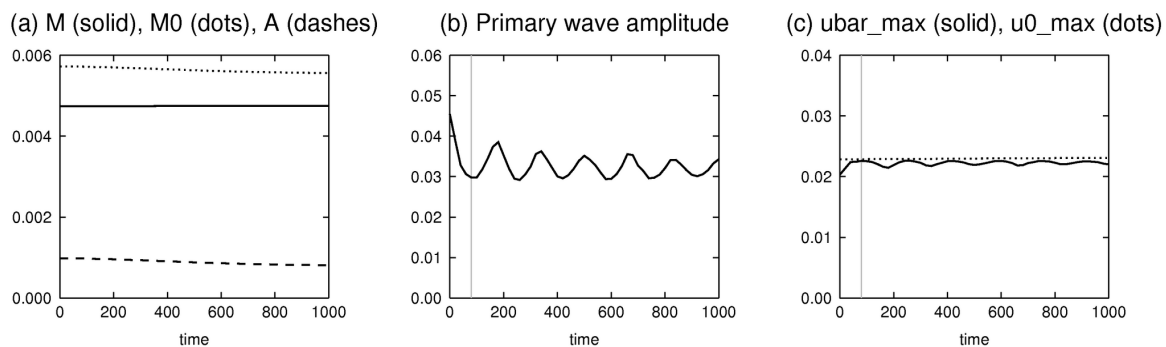


Figure 2: Timeseries of diagnostics from the simulation shown Figure 1: (a) M (solid), M_0 (dots) and \mathcal{A} (dashed), (b) the primary wave amplitude, defined as the root mean square displacement of the $q = 0$ contour, and (c) the maximum magnitudes of the zonal mean zonal wind \bar{u} (solid) and reference state zonal wind u_0 (dots). The vertical lines in panels (b) and (c) indicate the time $t = 80$.

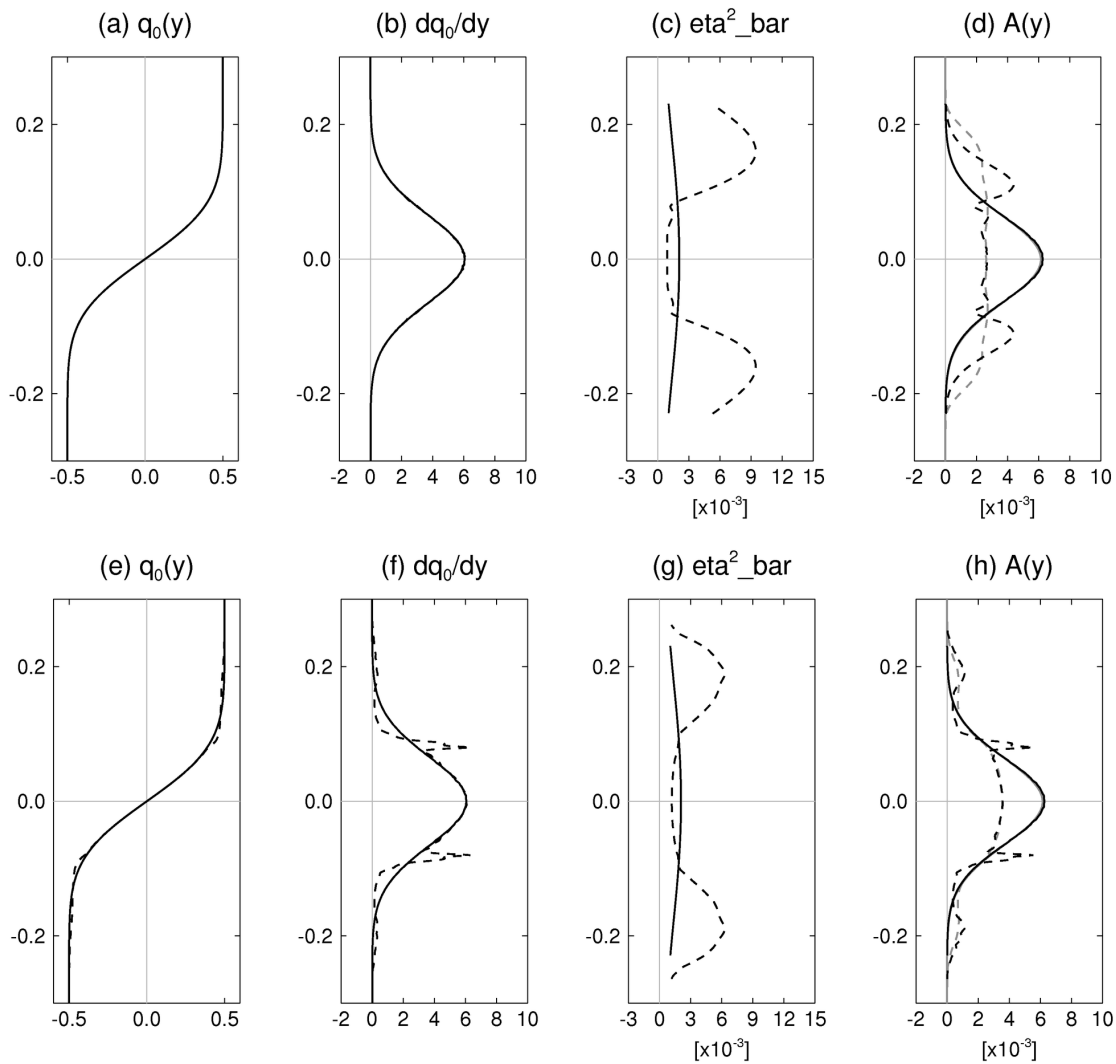


Figure 3: Meridional profiles of diagnostics from the simulation shown in Figure 1: (a, e) q_0 , (b, f) dq_0/dy , (c, g) $\overline{\eta^2}$, and (d, h) $A(y)$ (black) and $A_{NZ}(y)$ (grey). The solid lines show the initial condition and the dashed lines show times (upper row) $t = 80$ and (lower row) $t = 1000$.

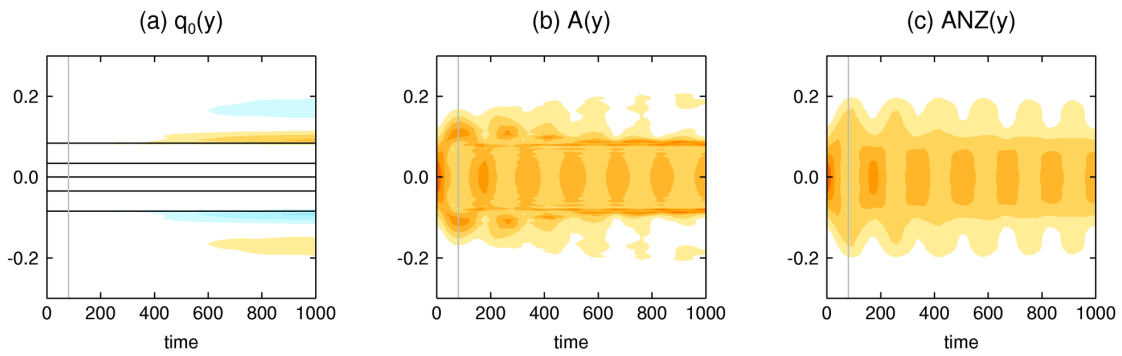


Figure 4: Diagnostics plotted a function of (y, t) from the simulation shown Figure 1: (a) q_0 (contours) and its departure from its value at $t = 0$ (shading), (b) $A(y)$, and (c) $A_{NZ}(y)$. The vertical lines indicate the time $t = 80$.

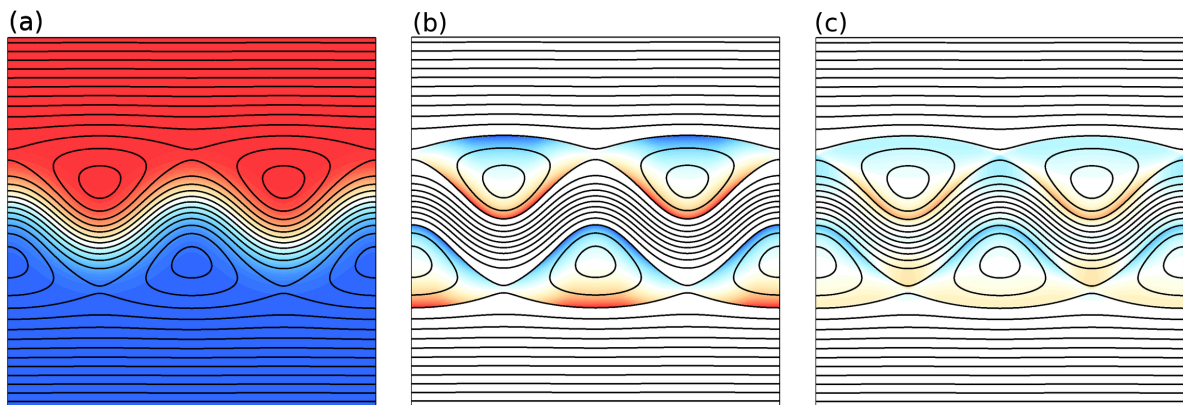


Figure 5: (a) The initial condition PV field for the simulation shown in Figure 1 (colours) together with the streamfunction computed in the frame of reference moving with the wave, as described in the text (lines). (b) The PV field generated by artificially rearranging PV values around the closed streamlines, q_{con} , and (c) the PV field generated by artificially mixing PV values along all streamlines, q_{mix} . Colours in panels (b) and (c) show PV anomalies relative to panel (a) and the lines show the same field as (a) for reference.

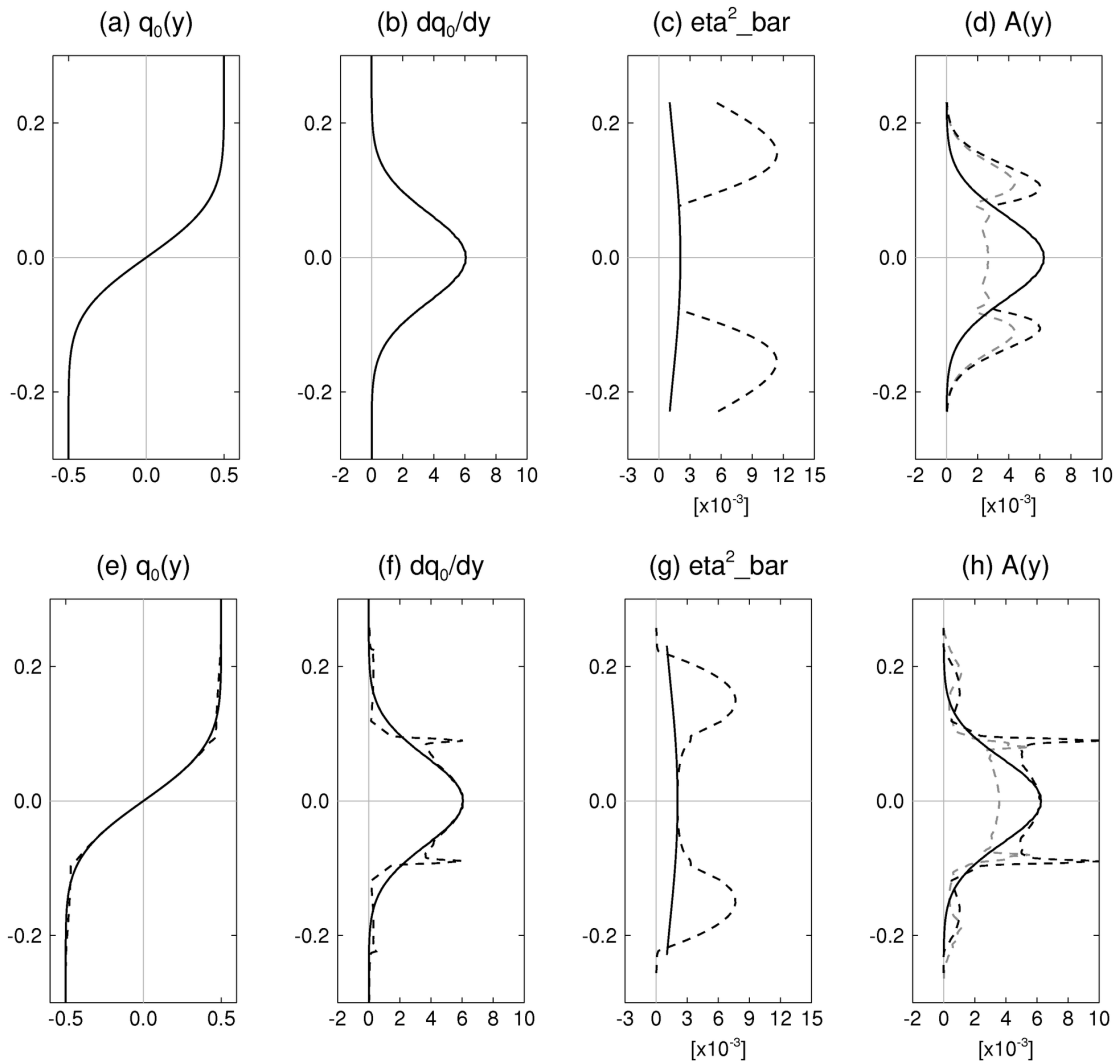


Figure 6: The same meridional profiles as Figure 3, but evaluated for the artificially-generated PV fields: (upper row) q_{con} , (lower row) q_{mix} . In addition, the grey lines in panels (d) and (h) show the profiles of $A(y)$ from the full simulation for comparison, with panel (d) showing time $t = 80$ (as in Figure 3(d)) and panel (h) showing time $t = 1000$ (as in Figure 3(h)). All panels show the initial (solid) and the modified (dashed) fields.

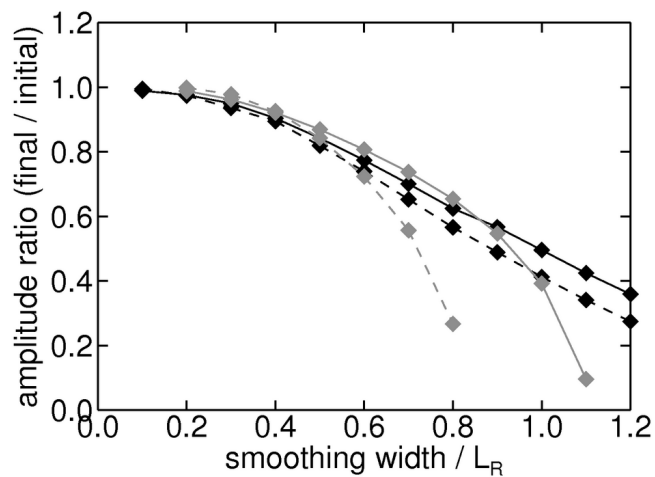


Figure 7: A summary of the suite of experiments. The fractional reduction in primary wave amplitude λ from the numerical simulations (black) and as estimated from the artificially modified PV fields (grey). The solid lines show the average wave amplitude during times $t = 800 - 1200$ from the simulations and the estimate based on the mixing PV values along all streamlines. The dashed lines show the wave amplitude at its first local minimum from the simulations and the estimate based on rearranging PV values around the closed streamlines.

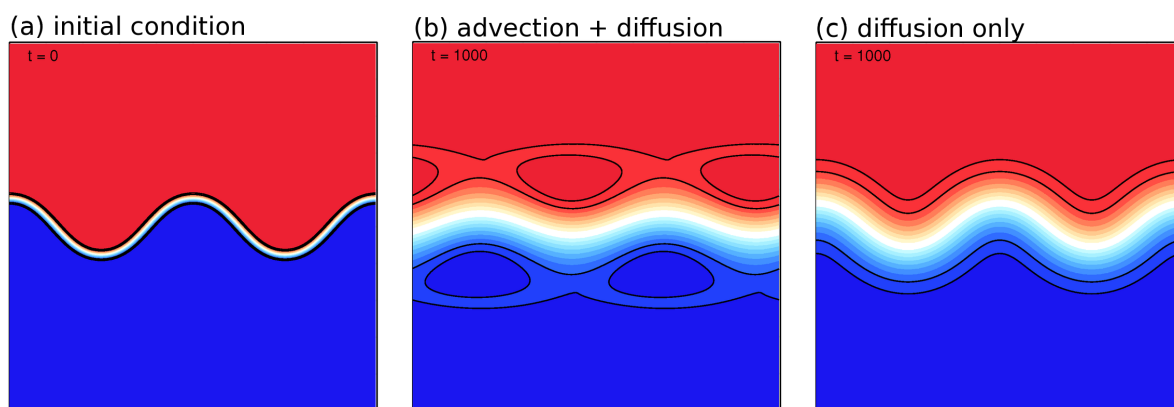


Figure 8: The PV field for an example simulation with diffusion parameter $\kappa = 2 \times 10^{-6}$ at times (a) $t = 0$, and (b) $t = 1000$. Panel (c) shows the time $t = 1000$ state for the corresponding simulation with advection switched off (see text). In each panel the two outermost contours are marked by solid lines for clarity.

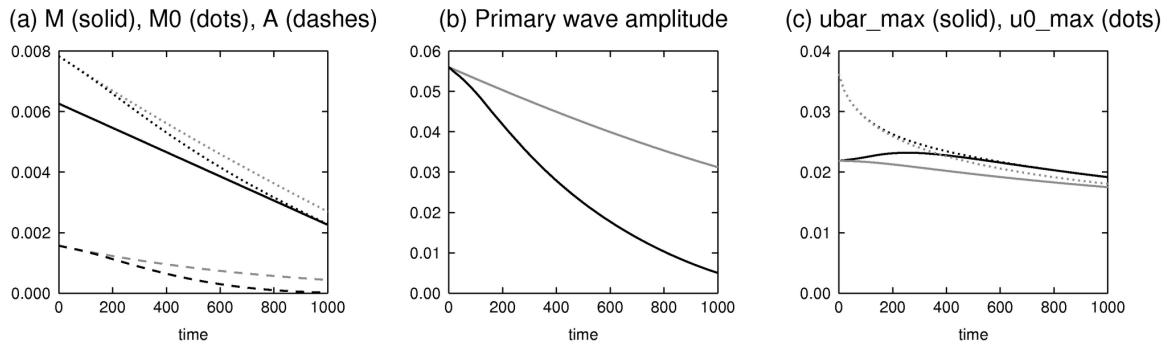


Figure 9: Timeseries of the same diagnostics as Figure 2 but for an example simulation with diffusion parameter $\kappa = 4 \times 10^{-6}$ (black lines). The grey lines show the corresponding simulation with advection switched off.

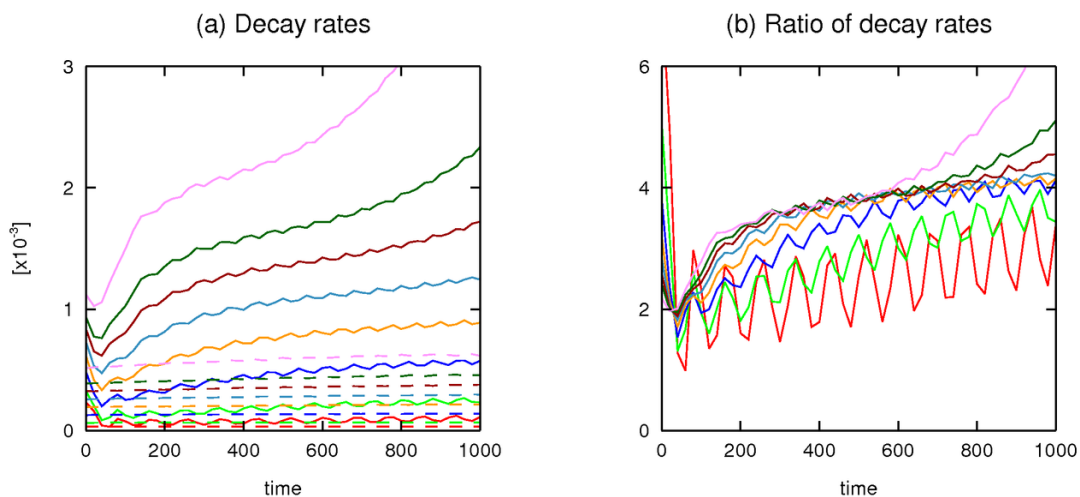


Figure 10: (a) Timeseries of the decay rate of primary wave amplitude for the full suite of diffusion experiments with $\kappa = (0.25, 0.5, 1.0, 1.5, 2.0, 2.5, 3.0, 4.0) \times 10^{-6}$ (solid, with decay rates increasing with κ) and the corresponding simulations with advection switched off (dashed). (b) The decay rates of primary wave amplitude in the full experiments divided by the same quantity in the corresponding simulations with advection switched off.

Table 1: Diagnostics from the simulation shown in Figure 1. Columns show the total zonal momentum of the MLM reference state (Equation (10)), the total zonal momentum of the full state (Equation (3)), and the global pseudo-momentum wave activity (Equation (12)). The first two rows show the numerical simulation at times $t = 80$ and $t = 1000$, and the bottom two rows show the two artificially-generated PV distributions described in the text. All values indicate differences from the initial condition.

	ΔM_0	ΔM	$\Delta \mathcal{A}$
Numerical simulation, $t = 80$	0.00	0.00	0.00
Numerical simulation, $t = 1000$	-2.01	0.15	-2.16
Artificially-generated PV, q_{con}	0.00	-5.99	5.99
Artificially-generated PV, q_{mix}	-1.79	-4.58	2.79